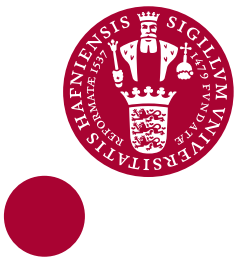

Electrochemical Fabrication and Characterization of Palladium Nanowires in Nanoporous Alumina Templates

Larsson, Alfred; Abbondanza, Giuseppe; Linpé, Weronica; Carlà, Franceso; Mousley, Philip; Hetherington, Crispin; Lundgren, Edvin; Harlow, Gary S.

Published in:
Journal of the Electrochemical Society

DOI:
10.1149/1945-7111/abb37e

Publication date:
2020

Document version
Publisher's PDF, also known as Version of record

Journal of The Electrochemical Society

The Electrochemical Society
Advancing solid state & electrochemical science & technology

Electrochemical Fabrication and Characterization of Palladium Nanowires in Nanoporous Alumina Templates

To cite this article: Alfred Larsson *et al* 2020 *J. Electrochem. Soc.* **167** 122514

Journal of The Electrochemical Society, 2020 **167** 122514

Electrochemical Fabrication and Characterization of Palladium Nanowires in Nanoporous Alumina Templates

Alfred Larsson,[1,2,z] Giuseppe Abbondanza,[1,2] Weronica Linpé,[1,2] Franceso Carlà,[3] Philip Mousley,[3] Crispin Hetherington,[2,4] Edvin Lundgren,[1,2] and Gary S. Harlow[1,2,5,z]

[1]*Division of Synchrotron Radiation Research, Lund University, 221 00 Lund, Sweden*
[2]*NanoLund, Lund University, 22100 Lund, Sweden*
[3]*Diamond Light Source, Didcot, United Kingdom*
[4]*National Center for High Resolution Electron Microscopy Lund University, 221 00 Lund, Sweden*
[5]*Department of Chemistry, Nano-Science Center, University of Copenhagen, DK-2100 Copenhagen Ø, Denmark*

A method for the electrochemical synthesis of palladium nanowires, using porous alumina templates with diameters of 25 nm and 40 nm, is presented. Through an electrochemical barrier layer thinning step, pulsed electrodeposition can take place directly into the anodized aluminum; without need for extra removal, pore opening, and metal contact coating steps. A digital oscilloscope is used to record and integrate the current, allowing the efficiency of the electrodeposition to be calculated. We discuss how using a large "off period" allows for the replenishment of the depleted diffusion layer. The nanowires are characterized by using a focused ion beam (FIB) to create cross-sections which can be accessed with a scanning electron microscope (SEM). With grazing-incidence X-ray diffraction (GI-XRD) we find that the nanowires have a slight compressive strain in the direction that they are confined by the pores (0.58% and 0.51% for the 25 nm and 40 nm pores respectively). Knowing the strain state of the nanowires inside the template is of importance for the use of templated nanowires in devices. Further characterization is made using high-resolution transmission electron microscopy (HR-TEM) and energy dispersive X-ray spectroscopy (EDS), after removal from the alumina templates.

 [DOI: 10.1149/1945-7111/abb37e]

Manuscript submitted June 27, 2020; revised manuscript received August 12, 2020. Published September 7, 2020.

Supplementary material for this article is available online

Controlled fabrication of well-ordered nanostructures over a large area is relevant in many fields of science and technology. Conventionally lithographic techniques are used to create templates for fabrication of nanostructures.[1] With electron beam lithography, 10 nm features can be defined with a high flexibility in terms of shape, but with a limited throughput. With Extreme UV lithography and nanoimprint lithography large areas can be exposed simultaneously with a resolution limit of around 10 nm and 5 nm respectively.[2,3] A potential cost effective alternative to the traditional lithography methods, is to use nanoporous alumina as a template for nanoscale fabrication.[4,5]

Anodization of aluminum, under certain conditions, can yield large aspect ratio nanopores with a pore diameter in the range of 10–200 nm [6] and pore depth of several μm.[7] The nanopores can self-organize into a hexagonal pattern, using a two-step anodization method [8]; and this porous oxide can in turn be used as a template for the fabrication of nanostructures. The material grown inside these porous templates takes the shape of the template resulting in ordered arrays of nanodots or nanowires. A "bottom-up" approach for growing nanostructures, within these nanoporous templates, is electrodeposition. The nanostructures are grown atom by atom, where the metal ions from the electrolyte are electrochemically reduced at the bottom of the pores. Electrodeposition into nanoporous alumina has been used to fabricate metallic nanowires of: nickel,[9] silver,[10] gold,[11] cobalt,[12] copper[13] and palladium,[14–17] among others. Nickel and cobalt nanowires are used for applications such as, magnetic storage [18] whereas palladium nanowires have been used as hydrogen gas sensors[15] and electro catalysts in direct alcohol fuel cells[17] and in biofuel cells.[14,19]

For electrodeposition directly into the nanoporous alumina templates to be possible, some modification of the template is needed. Growth of the nanoporous alumina film, through anodization, results in an oxide barrier layer at the bottom of the pores that separates the pores from the underlying aluminum. The electrically insulating property of the barrier layer therefore makes it difficult to fill the pores by electrodeposition. There are two main strategies to circumvent this. In the first method, the aluminum substrate underneath the nanoporous film is etched away to form a nanoporous membrane, which can be opened by a chemical etch. At one side of such a membrane, a contact can be evaporated and the nanoporous template can then be filled by DC electrodeposition.[20] However, this method increases the complexity of the fabrication process by adding additional processing steps. The second method is to make the barrier layer thinner.[21] This can be done either by chemical etching or electrochemical methods. Phosphoric acid is often used to etch the nanoporous alumina template resulting in a thinner barrier layer, but also a larger pore diameter since the wet etch is isotropic.[22] During electrochemical barrier layer thinning, the potential is lowered at the end of the last anodization step. Many of the physical parameters of the nanoporous template depend on the anodization potential, for example the pore diameter, interpore distance and barrier layer thickness.[7] By reducing the potential at the end of the anodization, the bottom of the pores branches out in a dendritic fashion resulting in smaller pores with a thinner barrier layer.[23]

Once the template is prepared, several strategies can be used to electrochemically deposit nanowires into nanoporous alumina. Even after barrier layer thinning, there is still a thin oxide layer that acts as an insulator between the electrolyte and the aluminum contact. Therefore, DC electrodeposition is often not suitable. Instead AC electrodeposition or pulsed electrodeposition can be used. Mass transfer however leads to limitations for AC deposition due to the slow recovery of electroactive species at the bottom of the pores. It has been shown through theoretical models that even at slight over potentials the deposition is mass transfer limited.[24] Also, the diffusion of ionic species through the nanopores is slower than in the bulk electrolyte.[25,26] For this reason, pulsed deposition is often used to allow the metal ion concentration to replenish at the bottom of the pores between each depositing cycle. The off-time between

[z]E-mail: alfred.larsson@sljus.lu.se; gary.harlow@chem.ku.dk

pulses is an important parameter that influences the filling ratio and grain size of the deposits.[27]

We have previously studied the self-assembly of nanoporous alumina using time resolved gracing incidence X-ray small angle scattering [28,29] and the deposition of tin nanowires into nanoporous alumina templates in situ using synchrotron techniques.[30,31] In this paper, arrays of self-organized alumina nanopores have been fabricated and used as a template for the bottom-up fabrication of palladium nanowires. The nanoporous alumina templates are initially created through a two-step anodization process and the barrier layer is made thinner by electrochemical barrier layer thinning. The palladium nanowires are grown using pulsed electrodeposition from a neutral palladium containing electrolyte, to avoid template dissolution, and a digital oscilloscope was used to record and integrate the current during the nanowire growth. The morphology of the palladium nanowires was investigated using a focused ion beam (FIB)/scanning electron microscopy (SEM) dual beam system and high-resolution transmission electron microscopy (HR-TEM). The elemental purity of the palladium nanowires was assessed using energy dispersive spectroscopy (EDS). The crystal structure was studied with X-ray diffraction (XRD) both in grazing incidence geometry (GI-XRD) and specular-reflection geometry. From XRD, grain size and strain could be calculated along and perpendicular to the growth direction. For nanowires grown inside nanoporous alumina templates, to be used in devices and applications, knowing the structure and strain state of the nanowires could potentially allow for template induced tailoring of their properties.

Experimental Methods

Fabrication of nanoporous alumina template.—The nanoporous alumina templates where fabricated through a two-step anodization of polycrystalline aluminum discs (purchased from SPL) polished to a mirror finish. To vary the pore diameter, two different aqueous electrolytes (in ultra-pure water, Millipore™) were used. To fabricate nanopores with a pore diameter of 25 nm, 0.3 M sulfuric acid was used with an anodization potential of 25 V. For fabrication of nanoporous templates with a pore diameter of 40 nm, 0.3 M oxalic acid with an anodization potential of 40 V was used. Before the first anodization, the aluminum samples where cleaned with acetone and ethanol and coated with an insulating polymer to only expose the polished side to the electrolyte. The samples were then anodized for 10 h. The electrolyte was kept at 0 °C using a jacketed electrochemical cell (Gammry*MultiPort Corrosion Cell)* connected to a refrigerating oil bath and stirred using a magnetic stir bar. After the first anodization step the samples were immersed in a mixture of chromic acid and phosphoric acid (0.185 M CrO_3 and 0.5 M H_3PO_4) overnight to remove the oxide layer that was formed during the first anodization step, this reveals concavities in the aluminum surface that during the second anodization guide the ordering of the pores. The second anodization step was performed under the same potential and temperature conditions and in the same electrolytes as the first anodization steps for 1 h. After the second anodization step, electrochemical barrier layer thinning was performed where the potential was linearly reduced. Barrier layer thinning in sulfuric acid was done by linearly decreasing the potential from 25 V to 1 V during 30 min. Barrier layer thinning in oxalic acid was done by linearly decreasing the potential form 40 V to 20 V over 30 min and then from 20 V to 1 V over 40 min. The fabrication steps used to grow the palladium nanowires are schematically shown in Fig. 1. Figures 2a and 2d shows the applied potential during the second anodization step in sulfuric and oxalic acid respectively and Figs. 2b and 2e shows the measured current during the second anodization step. The initial exponential decay of the current corresponds to the formation of a barrier type oxide followed by a minimum and an increase in the current which correspond to the formation of the porous oxide. The steady state regime of the current corresponds to further steady-state growth of the porous oxide film. During the barrier layer thinning step, the current decrease to zero. Figures 2c and 2f show SEM images of the porous structures formed in sulfuric and oxalic acid with pores ordered in a hexagonal pattern. The pores have diameters of 25 nm or 40 nm, according to the conditions described above.

Electrodeposition of palladium nanowires.—Electrodeposition was performed using a neutral electrolyte containing $Pd(NH_3)_4Cl_2$ and NH_4Cl. The neutral pH of the electrolyte was selected to avoid the dissolution of the porous alumina template during deposition.[32] The solution was produced by dissolving palladium chloride in a solution containing hydrochloric acid and slowly pouring that into a solution containing ammonium hydroxide to produce $Pd(NH_3)_4Cl_2$ and NH_4Cl. The pH was then adjusted to 8 by adding dilute ammonia and dilute hydrochloric acid. To make the solution, 16.2 mM $PdCl_2$, M HCl and 0.81 M NH_4OH was used. $Pd(NH_3)_4Cl_2$ and NH_4Cl is a well-established electrolyte for palladium electroplating.[33]

Pulsed electrodeposition was used to grow the palladium nanowires. The pulse shape was square, and each pulse cycle started with a depositing pulse of 5 ms at −10 V followed by a 5 ms pulse of 10 V used to discharge the capacitance of the barrier layer.[9] The two pulses were followed by an off time at 0 V for 190 ms, resulting in a duty cycle of 0.025.[34] The electrodeposition was performed at room temperature with a graphite counter electrode and the electrolyte was continuously stirred using a magnetic stirring bar. A digital oscilloscope with a time resolution of 1 ms was used to record the current and potential signal during the electrodeposition.

SEM.—After electrodeposition and rinsing, a Nova NanoLab 600 dual beam (FIB/SEM) from FEI Company was used to study the morphology of the palladium nanowires from a cross-section view inside the nanoporous structure. The FIB was used to mill away material from the nanoporous oxide film and the underlying aluminum. This formed a trench exposing a cross-sectional view of the nanoporous film. Prior to FIB milling, a strip of platinum was deposited using FIB assisted platinum deposition. This was done to protect the nanowires inside the nanoporous alumina from the ion beam and to give a smooth cross-section cut. After milling away material with the FIB the nanoporous structure and the embedded palladium nanowires were studied using the SEM in the dual beam system. The SEM was operated at 10 kV in backscattering electron collection mode. When imaging the cross-section of the nanoporous oxide the sample is tilted 52 degrees relative to the normal plane of the electron beam. Knowing this angle, the true height of the pores and the nanowires can be calculated as $h = y/\sin(52)$, where h is the real height and y is the measured height in the image.

TEM/EDS.—HR-TEM and EDS were performed using a JEM-3000F analytical high-resolution TEM operated at 300 kV, to study the morphology, crystal structure and chemical composition of individual palladium nanowires after electrodeposition. To prepare samples for TEM the fabricated palladium nanowires were released from the nanoporous template by dissolving the alumina in 1 M NaOH. To collect as many nanowires as possible a centrifuge was used to accelerate the sedimentation of the nanowires. The nanowires were then rinsed several times in ultrapure water and stored in ethanol. To separate the aggregates of nanowires in the ethanol solution a vial containing the nanowires suspension was submerged in an ultrasonic bath for 15 min. A 20 μl droplet of nanowire suspension was placed on a TEM copper grid where the solvent evaporated to leave free nanowires suitable for TEM analysis. Image analysis was done using ImageJ.[35]

XRD.—To study the grain size and strain state of the nanowires embedded in the template XRD was performed in two geometries at beamline I07, Diamond Light Source, UK. The sample was mounted on a 2 + 3 circle diffractometer, as described elsewhere,[36] and a DECTRIS Pilatus 100 K detector was used to collect the scattered X-rays. The energy of the incoming X-ray beam was 25 keV, with a

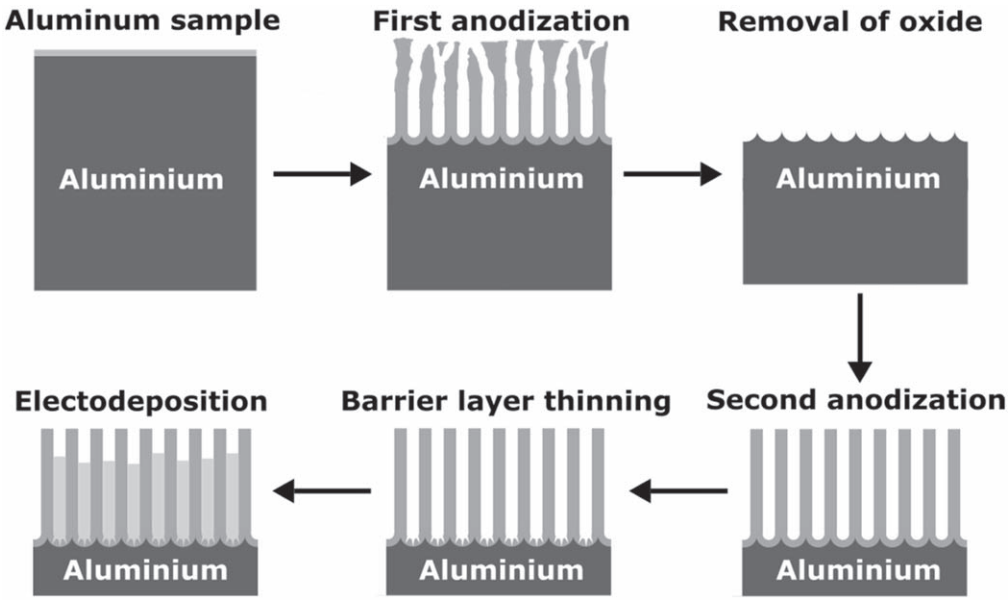

Figure 1. Schematic illustration of the sample during the fabrication steps used to grow palladium nanowires. The two-step anodization includes, the first anodization, the removal of the oxide and the second anodization. Prior to electrodeposition, the barrier layer was made thinner by gradually lowering the potential at the end of the second anodization step. Palladium nanowires were then grown by pulsed electrodeposition.

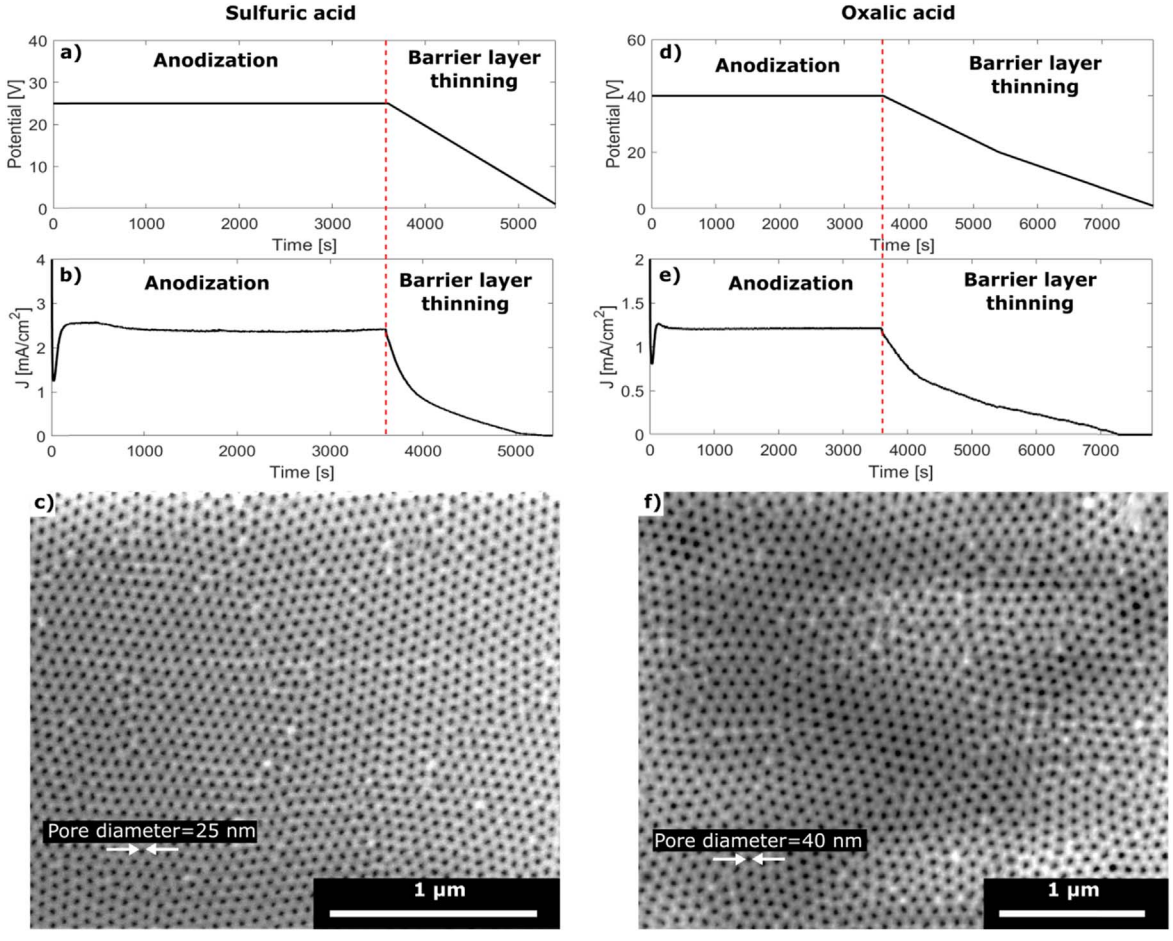

Figure 2. Anodization potential and current during the second anodization step in sulfuric acid and oxalic acid. Also shown are SEM images from the top of the templates after anodization. (a) Anodization potential for sulfuric acid. (b) Anodization current for sulfuric acid. (c) SEM image of the top of the porous structure formed after a 2nd anodization in sulfuric acid. (d) Anodization potential in oxalic acid. (e) Anodization current in oxalic acid. (f) SEM image showing a top view of the porous structure formed after a 2nd anodization in oxalic acid.

beam size of 100 μm (vertical) $\times$ 300 μm (horizontal) at the sample position. A Si standard was used to calibrate the diffractometer.

Strain is always measured parallel to the scattering vector **Q**, which is defined as the outgoing wavevector, $\mathbf{K_{out}}$, minus the incoming wavevector, $\mathbf{K_{in}}$ ($\mathbf{Q} = \mathbf{K_{out}}–\mathbf{K_{in}}$). To measure the grain size and lattice parameter along the growth direction of the nanowires XRD was performed in a specular-reflection geometry where the **Q** vector always is normal to the plane of the sample surface. This was done by scanning the incidence angle α and the detector out of plane along the angle δ, in a θ–2θ scan in angular steps of 0.05 degrees and 0.1 degrees respectively with an exposure time of 1 s. To measure the grain size and strain perpendicular to the growth direction (in the plane of the sample surface) Grazing Incidence-XRD (GI-XRD) was performed, at an incidence angle of $\alpha = 0.1$ degrees, and the detector was scanned in the plane of the sample surface along γ with an angular step of 0.1 degrees and exposure time of 1 s. For GI-XRD, the information depth is here calculated as the 1/e depth, which defines a volume confined by the information depth from which 63% of the diffraction signal originates from.[37] For porous alumina (Al_2O_3 with around 13% porosity[38]) at 25 keV with an incidence angle of 0.1 degrees the information depth is 4.6 μm. This gives sufficient penetration to measure diffraction form the nanowires embedded in the nanoporous alumina templates.

The 2-D detector images where integrated by assigning each pixel a δ and γ value as described by Ref. 39 then 2θ for each pixel was calculated as $2\theta = \arccos(\cos[\gamma_{pixel}] * \cos[\delta_{pixel}])$. The intensity of each pixel was corrected for the difference in sample to detector distance and the projected pixel size as described in Ref. 39.

Results and Discussion

Templated nanowires.—Palladium nanowires were grown inside the nanoporous templates via pulsed electrodeposition, filling the pores from the bottom up. Figures 3a and 3b show cross-sectional view SEM (backscattered electron) images of the palladium nanowires, inside the nanoporous oxide films for the 25 nm pore size template (sulfuric acid anodized) and Figs. 3c and 3d show the 40 nm template (oxalic acid anodized). In Fig. 3 the nanoporous film containing the grown nanowires can be seen. Underneath the nanoporous film is the aluminum substrate, into which the nanoporous film was grown. On top of the nanoporous film a platinum strip can be seen that was used to protect the nanoporous oxide and the contained nanowires during the FIB processing. From the SEM images the depth of the nanopores can be measured. Anodization for one hour plus the electrochemical barrier layer thinning results in a thickness of ~4.4 μm for anodization in sulfuric acid and ~2.8 μm for anodization in oxalic acid. The difference in growth rate of the oxides is also reflected by a difference in the steady state current density during the anodization shown in Figs. 2b and 2e. For anodization in oxalic acid (at 40 V), which yielded more shallow pores, the steady state current is lower than for anodization in sulfuric acid (at 25 V).

Looking more closely at the nanowires inside the nanoporous templates in Figs. 3b and 3d, branching of the nanowires at the bottom can be seen. The nanowires adapt the shape of the pores and the growth is restricted in all directions except along the height of the pores. At the bottom of the pores, where the crystal growth is initiated, the nanowires grow through the branched pore bottoms formed during the electrochemical barrier layer thinning step. It can be seen in Figs. 3b and 3d that the branches extend longer for the sample anodized in oxalic acid than in sulfuric acid. This can be explained by the longer barrier layer thinning process time needed to achieve a similar barrier layer thickness in the end. As seen in Figs. 2a and 2d, a longer time is needed to lower the potential from 40 V than 25 V at a constant speed. This results in more growth and hence deeper branches when anodizing with this recipe in oxalic acid. The observed variation in the height of the nanowires, could be explained by a variation in the barrier layer thickness between pores, which might not be entirely homogeneous. For a certain applied potential, the current flowing will then be slightly different for each pore and the volume of deposited material will vary. The average nanowire height measured from the SEM images is around 1.3 ± 0.2 μm for the 25 nm template and 1.1 ± 0.3 μm for the 40 nm template.

Current efficiency and diffusion dynamics.—Figure 4a shows the (measured) applied potential pulses, and Figs. 4b and 4c shows the resulting current density flowing through the cell, i.e. during the electrodeposition into the 25 nm and 40 nm diameter templates. The current pulses follow the shape of the applied potential pulses and have an amplitude of around 50 mA cm^{-2} for the 25 nm template and 60 mA cm^{-2} for the 40 nm template. As can be seen, there is a decay of the current within the individual current pulses. This could be due to non-faradic processes such as charging of the double layer and the building up of capacitance in the barrier layer. Discharging the capacitance of the barrier layer is the purpose of the positive pulse in pulsed electrodeposition.[9,10] The barrier layer oxide will be connected in series between the electrolyte interface and the power supply from a traditional electrical circuit point of view. The barrier layer will contribute the same to the capacitive current regardless of the presence of the palladium. Hence, capacitive charging and discharging will take place during the entire growth process. Electrochemical Impedance spectroscopy was performed on the palladium nanowire sample after deposition and clear drop in impedance at higher frequency was observed due to the capacitance of the barrier layer oxide between the nanowires and the aluminum substrate (see supplementary information is available online at stacks.iop.org/JES/167/122514/mmedia), which is in agreement with the literature.[21,40,41] Faradic processes resulting in mass-transfer limitations can also contribute to the current decay during each pulse, similar to what the Cottrell equation predicts during a potential step experiment. The current pulses, where the negative pulses correspond to the depositing phase, were integrated to give the total cathodic and anodic charge transferred during the deposition. The total cathodic and anodic charge transferred, as a function of time, is given in Figs. 4d and 4e for deposition into the 25 and 40 nm template. As seen in the figure, there is a net difference between the total cathodic and anodic charge transferred. This difference is interpreted as the cathodic charge that has been supplied and resulted in nanowire growth. From this a theoretical height of the palladium nanowires can be calculated assuming a 100% current efficiency. The nanowire height, h, can then be calculated using a modified Faradays law as shown in Eq. 1

$$h = \frac{QM}{n\rho AF} \qquad [1]$$

where Q is the number of coulomb transferred, M is the molar mass of palladium, n is the number of electrons needed to reduce a palladium ion, ρ is the density of palladium, A is the base area of the palladium nanowires and F is faradays constant. For Pd^{2+} ions n = 2 and for nanoporous alumina the base area of the nanowires is equal to the porosity which is around 10%.[38] The actual measured porosity differs slightly from 10%. For the 25 nm template the porosity was measured to be 12% giving a base area of $A = 0.12A_{geo}$, where A_{geo} is the geometrical area of the sample. For the 40 nm template the measured porosity is 14% resulting in a base area of $A = 0.14A_{geo}$. Therefore, a nanowire height of 3.8 μm per coulomb and cm^2 is expected for the 25 nm template and 3.3 μm per coulomb and cm^2 is expected for the 40 nm template. This can be compared to the difference between the cathodic and anodic charge, transferred during the deposition of the nanowires, and the measured height of the nanowires from SEM. The difference between the cathodic and anodic charge transferred during the deposition was 0.4 ± 0.1 C cm^{-2} for the 25 nm diameter template and 0.9 ± 0.1 C cm^{-2} for the 40 nm diameter template. Assuming a 100% current efficiency this would result in a nanowire height of 1.5 μm and 3 μm respectively. When comparing this value to the experimentally measured heights (1.3 μm and 1.1 μm), the cathodic current efficiency of the deposition process can be evaluated (by calculating the ratio between the

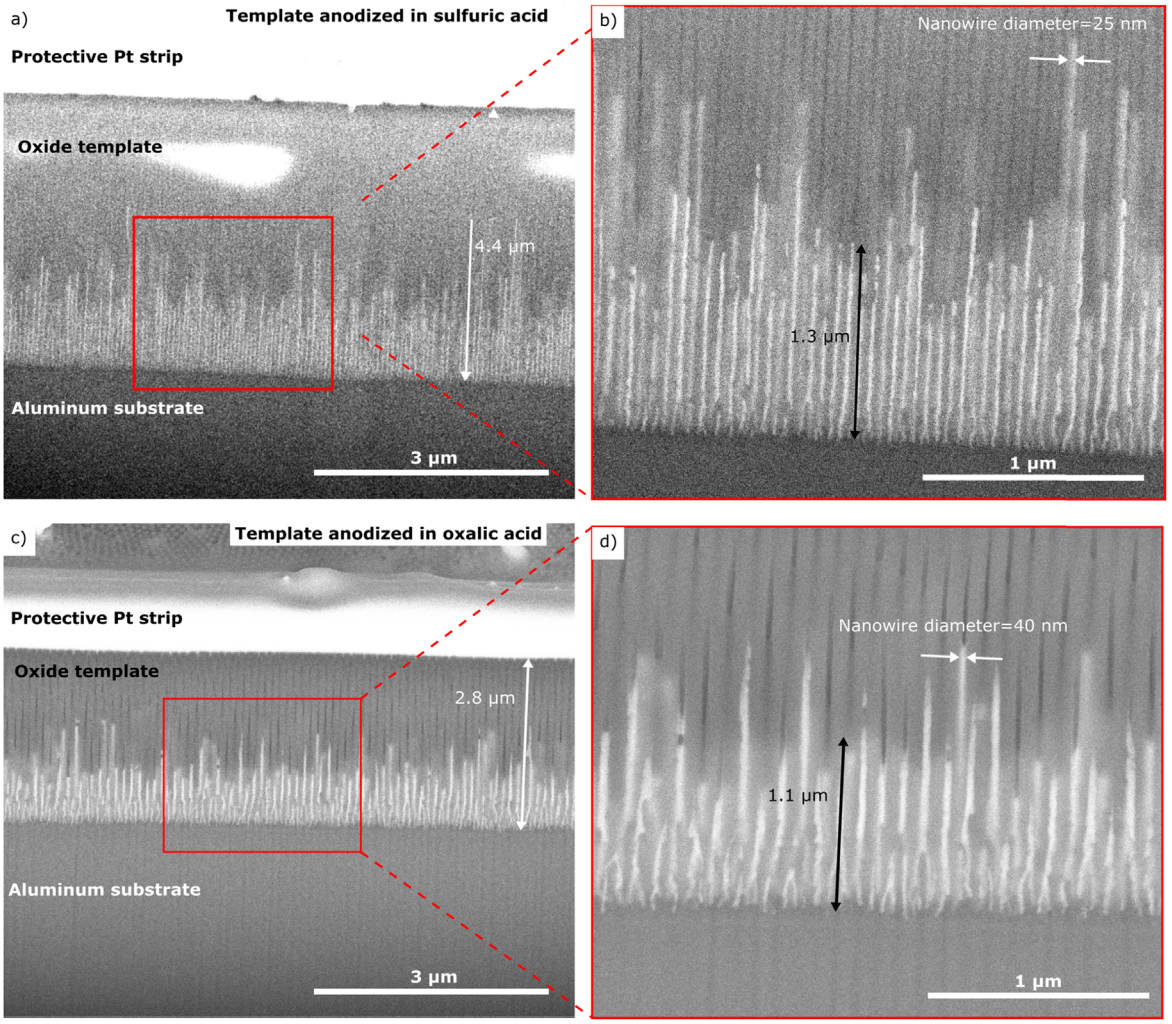

Figure 3. (a) SEM (backscattered) images of palladium nanowires inside the 25 nm nanoporous oxide film anodized in sulfuric acid. (b) Magnified image of the area marked with red box in (a). (c) SEM images of palladium nanowires inside the 40 nm nanoporous oxide film anodized in oxalic acid. (d) Magnified image of the area marked with red box in (c).

measured height and the theoretical height). This results in a cathodic current efficiency of ~70% during the deposition in the 25 nm template and ~35% during deposition into the 40 nm template. The growth from one pulse can be calculated from the measured height with SEM and knowing the number of pulse cycles applied. For the pulses shown in Fig. 4 with a period of 200 ms the growth per pulse cycle is 1.0 Å for the 25 nm template and 0.8 Å for the 40 nm template. The lower current efficiency for the 40 nm template could be explained by other faradic side reactions occurring, such as hydrogen evolution. Cathodic side reactions are known to happen to the nanoporous oxide which may cause breakdown of and damage to the oxide.[9,42,43] Anodization of aluminum in different electrolytes influences the chemistry of the anodic oxides due to anion incorporation.[7] The different chemistry of the nanoporous oxide formed in oxalic acid and sulfuric acid may influence the side reactions that are taking place. Also the morphology of the pore bottoms may affect the current efficiency during the filling of the branches. Since the diameter of the branched pore bottoms is smaller than the regular pores, mass transfer should be more significant in the narrow branches. Hence, this would lower the current efficiency during the early stage while growth takes place in the branches. A similar argument could also explain the lower current efficiency of the 40 nm template since the range of the branched pore bottom extends longer for the 40 nm template than for the 25 nm template as shown in Fig. 3.

The ion consumption and the depletion volume of palladium ions near the nanowire/electrolyte interface during one growth pulse can be estimated. The concentration of palladium ions in the bulk electrolyte is 16 mM and here it is assumed that the concentration of ions inside of the pores is the same as in the bulk. It is then possible to calculate the depletion region, in depositing 1 Å, to be ~700 nm tall. This means that in one pore all the ions in the volume that stretches 700 nm above the nanowire/electrolyte interface will be consumed during the growth from one pulse.

Napolskii et al. measured the diffusion coefficient of Ni ions through alumina nanopores and determined that the diffusion coefficient of nickel cations in the pores to be 2×10^{-7} cm^2 s^{-1} which is 30 times lower than the diffusion coefficient in the bulk electrolyte.[26] It is known that the diffusion coefficient of cations inside nanoporous alumina is lower than in bulk electrolyte due to interactions with the pore walls.[25] Assuming that the diffusion coefficient of palladium cations is similar inside the alumina nanopores the time for palladium cations to diffuse 700 nm can be calculated using Einstein's theory of Brownian motion as shown in Eq. 2

$$x = \sqrt{2Dt} \qquad [2]$$

where x is the distance, D is the diffusion coefficient and t is the time. It would then take 12 ms for a palladium cation to diffuse 700 nm inside of the pores.

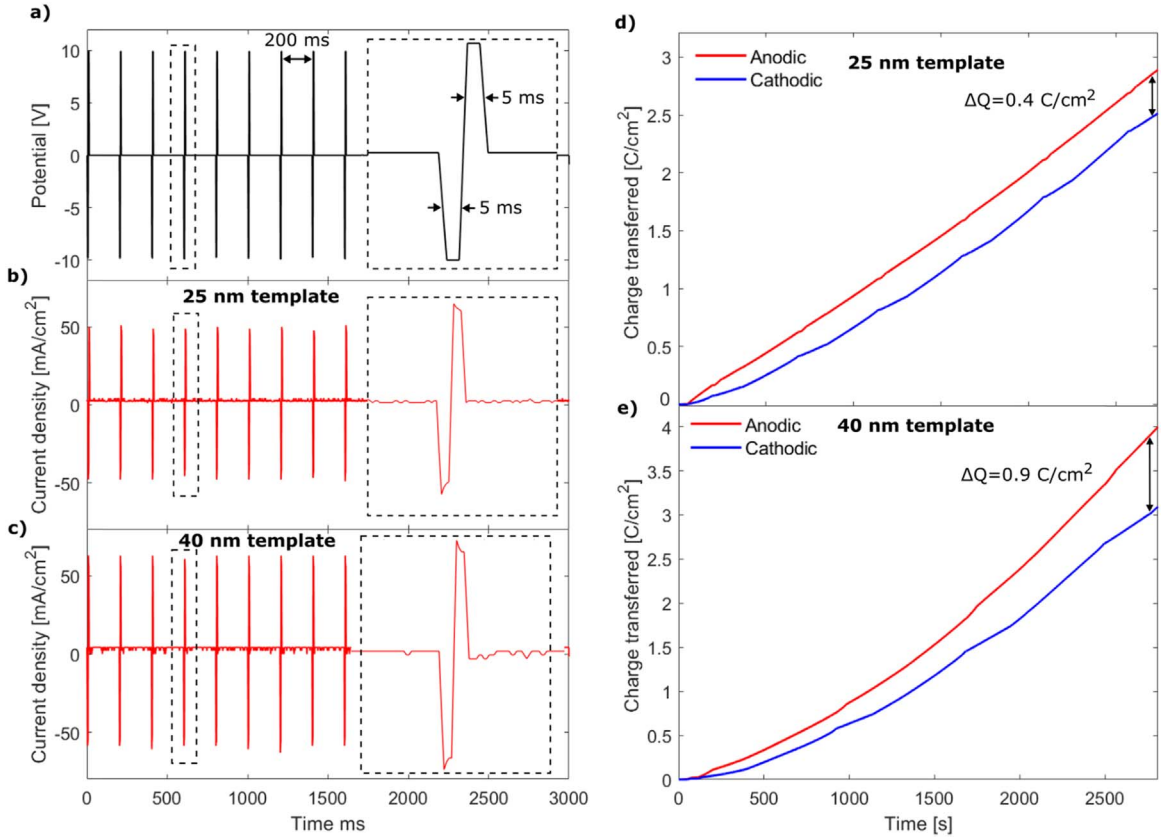

Figure 4. (a) Potential pulses applied during electrodeposition with 5 ms pulse duration, 10 V amplitude and 190 ms off-time between pulses. (b) Current density during the electrodeposition of palladium into the 25 nm diameter template anodized in sulfuric acid. (c) Current density during the electrodeposition of palladium into the 40 nm diameter template anodized in oxalic acid. (d) Integration of cathodic (negative) and anodic (positive) current density during deposition into 25 nm template (sulfuric acid anodized). (e) Integration of cathodic (negative) and anodic (positive) current density during deposition into 40 nm template (oxalic acid anodized). Integration of the current density gives the total anodic and cathodic charge transferred during electrodeposition.

The concentration of palladium cations in the pores during a growth pulse and then subsequent replenishment during off-time was simulated. This was performed by using analytical solutions to the one-dimensional form of Fick's second law of diffusion (as shown in the supplementary information). The simulation was performed with a diffusion coefficient of 2×10^{-7} cm^2 s^{-1}, as measured by Napolskii et al. for Ni^{2+} in nanoporous alumina matrix, which should be simmilar to the diffusion coefficient of Pd^{2+} in nanoporous alumina. Figure 5 shows the simulated palladium cation concentration profile for different times during the 5 ms cathodic pulse and then for the off-time. As seen, there is a depletion region above the nanowire/electrolyte interface, which grows larger as a function of time during the cathodic pulse, when palladium ions are consumed at the nanowire/electrolyte interface. After 45 ms the concentration of Pd cations is nearly replenished. However, since our simulation does not include the effects of migration and natural convection it does not fully converge even after 200 ms off-time. In reality, there is always convection present, which will replenish the concentration of palladium ions near the nanowire/electrolyte interface much faster.[44] This simulation illustrates the need for pulsed electrodeposition with relatively short pulse duration and long off times, due to mass transfer limitations caused by the low diffusion coefficient of cations in the nanoporous alumina.

Structure of pore-confined nanowires.—Synchrotron diffraction was performed in two geometries to measure strain and grain size parallel and perpendicular to the growth direction of the nanowires while still embedded in the nanoporous template. A specular reflection geometry (Fig. 6a) was used to study the grain size and strain along the growth direction of the nanowires, by aligning the Q vector with the normal of the sample surface. GI-XRD (Fig. 6b) was performed to measure the grain size and strain perpendicular to the growth direction where the Q vector lies in the plane of the sample surface. The palladium nanowires are assumed to have no rotational order in the plane of the sample surface. Figures 6c and 6d show the detector images of the palladium (111) reflection in and out of plane. As seen, it is a weak broad ring without texture, which illustrates that the palladium consists of small grains with no clear preferred orientation. The quality of the powder rings justifies the analysis of the diffraction data as a complete powder. Figures 6e and 6f shows the integrated XRD pattern measured out of plane (specular) and in the plane of the sample surface (GI-XRD) for e) nanowires grown in the 25 nm template and f) nanowires grown in the 40 nm template. The palladium peaks were indexed and fitted with a Lorentzian line profile indicated with red in the figure. The grain size was calculated from the line broadening of the Pd (111) reflections, since the other reflections were too weak out of plane. The grain size was calculated using Scherrer's Eq. 3 with $K = 0.9$ for spherical particles.

$$D_{hkl} = \frac{K\lambda}{B_{hkl}\cos(\theta_{hkl})} \quad [3]$$

The line broadening resolution, B_{res}, was calculated as described by[45] to take into account mainly the geometrical broadening from the large footprint of the incident X-ray beam along the sample surface being projected at the detector. For the GI-XRD geometry this results in a line broadening resolution $B_{res} = 0.0026$ rad. For the specular geometry the geometrical footprint was modified as shown in Eq. 4

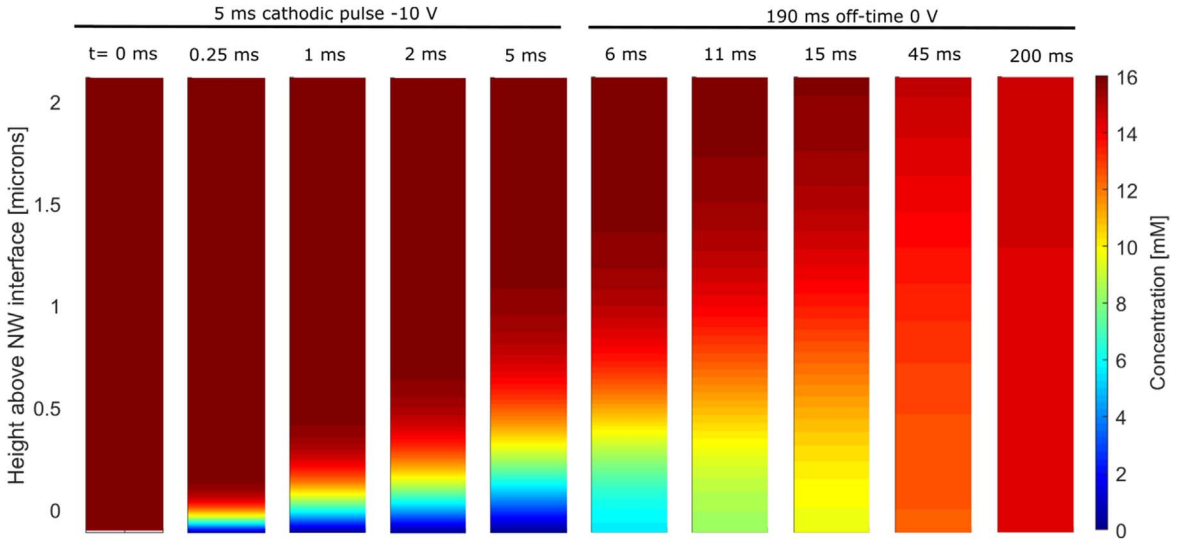

Figure 5. Simulated profile of Pd^{2+} above the nanowire (NW) interface during a 5 ms cathodic pulse and then a subsequent period of off-time. The simulation was performed using a measured diffusion coefficient of Ni^{2+} in nanoporous alumina matrix, which is expected to be similar to the diffusion coefficient of Pd^{2+} in the nanoporous alumina matrix.

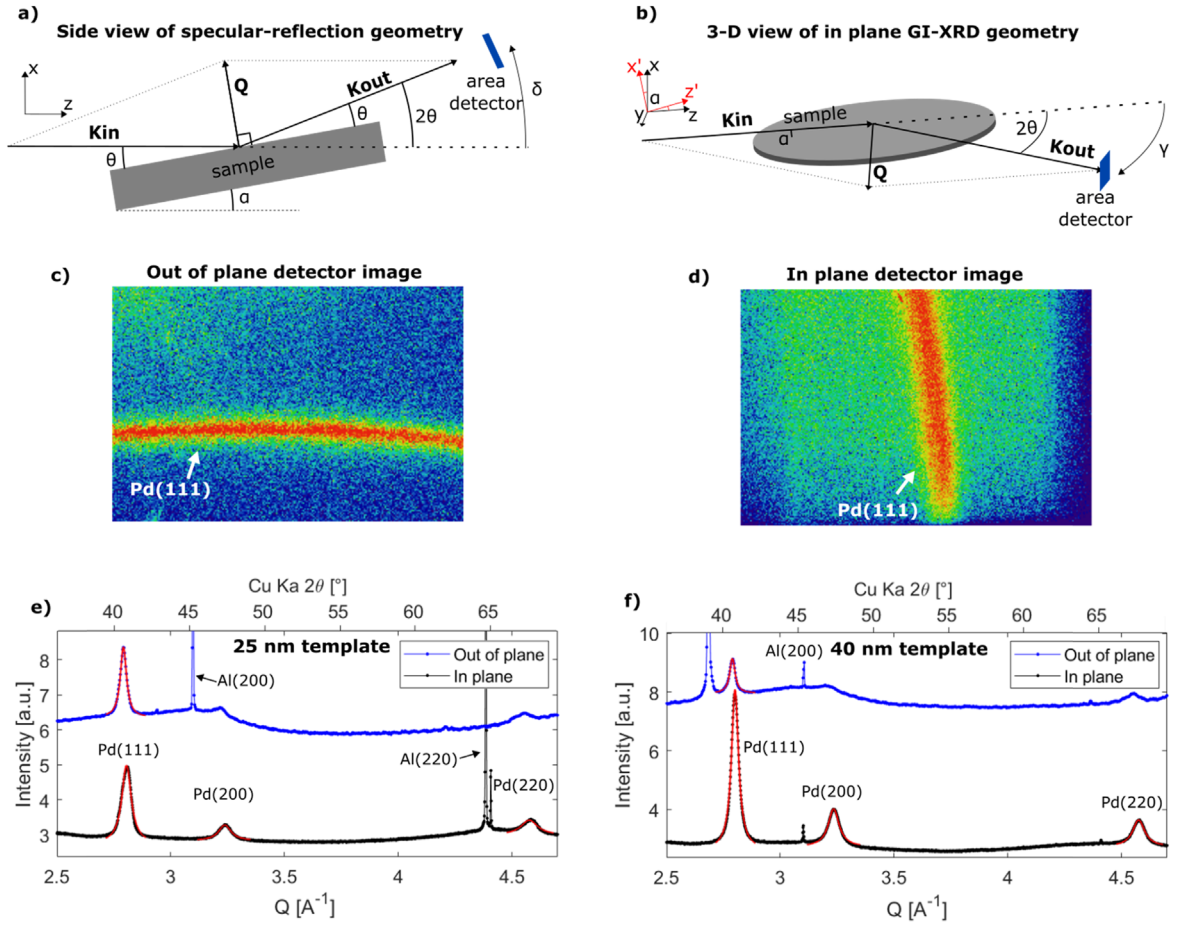

Figure 6. (a) Schematic illustration of specular reflection diffraction geometry. (b) Schematic illustration of grazing incidence diffraction geometry. (c) Out of plane detector image showing parts of the palladium (111) powder ring. (d) In plane detector image showing parts of the palladium (111) powder ring. (e) Integrated diffraction intensity for 25 nm template. (f) Integrated diffraction intensity for 40 nm template. Out of plane diffraction (Specular-reflection) plotted as blue and in plane diffraction (GI-XRD) plotted as black. The palladium Bragg peaks were fitted with a Lorentzian line profile shown as red. Bragg reflections from the aluminum substrate are also labelled.

$$B_{geo} = \frac{d_{vertical} \tan(\theta)}{\mathrm{Lsin}(\theta)} \quad [4]$$

where $d_{vertical}$ is the vertical beamsize, L is the sample to detector distance and θ is the Bragg angle. This results in a line broadening resolution $B_{res} = 7.7 \times 10^{-5}$ rad. The error of the grain size is here based on the 95% confidence interval from the Lorentzian fitting of the diffraction peaks. For the nanowires grown in the 25 nm template the average grains size was calculated to be 11.2 ± 0.35 nm in the plane perpendicular to the growth direction and 17.1 ± 0.38 nm along the growth direction.

For the nanowires grown in the 40 nm template the average grain size was calculated to be 15.6 ± 0.23 nm in the plane perpendicular to the growth direction and 20.0 ± 0.67 nm along the growth direction. Comparing the grain size measured from XRD to the amount of material grown from one pulse (as calculated above), it is seen that around 100 pulses are needed to grow one grain. For both sizes of templates studied, the grains are larger along the growth direction than across. We also see that the grain size is smaller for the nanowires grown in the smaller template. This clearly illustrates how the nanoporous template influences the crystal structure of nanowires grown by templated synthesis.

The strain of the nanowires were determined from the shift of the Pd (111) refection when comparing the measurements where the Q vector was parallel to the growth direction and perpendicular to the growth direction. For the measurements where the Q vector was perpendicular to the growth direction of the nanowires (GI-XRD), a shift in the peak position to higher Q was observed. The strain, ε, was calculated as shown in Eq. 5

$$\varepsilon = \frac{(D - D_0)}{D_0} \quad [5]$$

where D is the strained lattice plane spacing, D_0 is the unstrained lattice plane spacing taken here as the D spacing of relaxed bulk palladium, $a_{bulk} = 3.89$ Å. The error of the strain is here based on the 95% confidence interval from the Lorentzian fitting of the diffraction peaks. For the nanowires inside the 25 nm template, a compressive strain of −0.36 ± 0.02% perpendicular to the growth direction and a tensile strain of 0.21 ± 0.02% along the growth direction of the wires was found. For the nanowires inside the 40 nm template, there was a compressive strain of −0.22 ± 0.02% perpendicular to the growth direction and a tensile strain of 0.29 ± 0.02% along the growth direction of the wires. This illustrates an effect on the crystallographic structure of nanowires grown in nanoporous templates caused by the confinement of the template. The crystal lattice is expanded relative to the relaxed bulk lattice along the growth direction of the nanowire and contracted in the confined direction perpendicular to the growth direction. For the nanowires grown in the 25 nm template this results in a compressive strain of 0.58 ± 0.02% perpendicular to the growth direction compared to along the growth direction. For the nanowires grown in the 40 nm template the compressive strain is 0.51 ± 0.02%. This shows that compressive strain in the confined direction is higher for the nanowires grown in the templates with a smaller pore diameter. The electrochemical

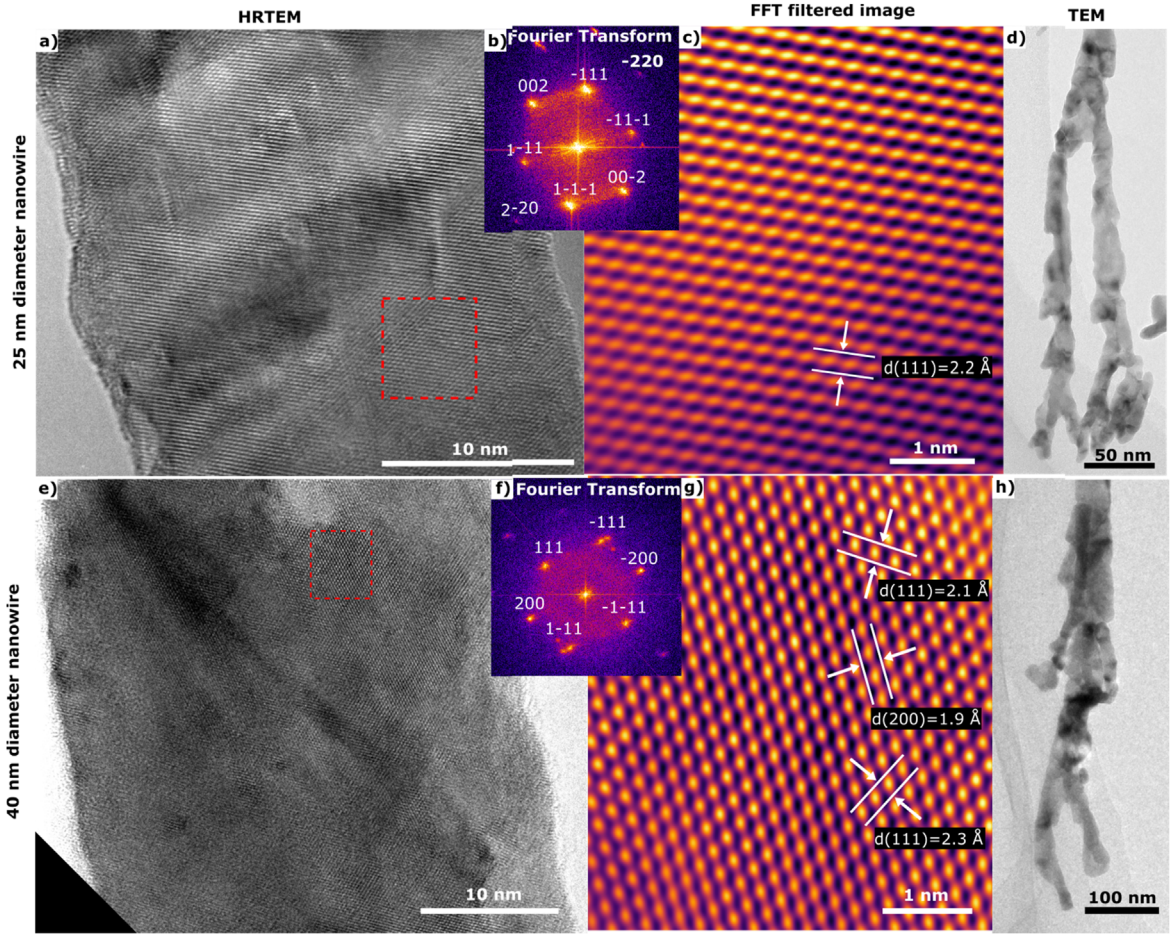

Figure 7. TEM images for 25 nm 40 nm diameter nanowire sample. (a) High resolution TEM image of free 25 nm diameter palladium nanowire. (b) Fourier transform of (a). (c) FFT filtered image from region within red box in (a). (d) TEM of branched structures of 25 nm nanowire formed at the bottom of the pores. (e) High resolution TEM image of free 40 nm diameter palladium nanowire. (f) Fourier transform of (e). (g) FFT filtered image from region within red box in (e). (h) TEM image of branched structures of 40 nm nanowire formed at the bottom of the pores.

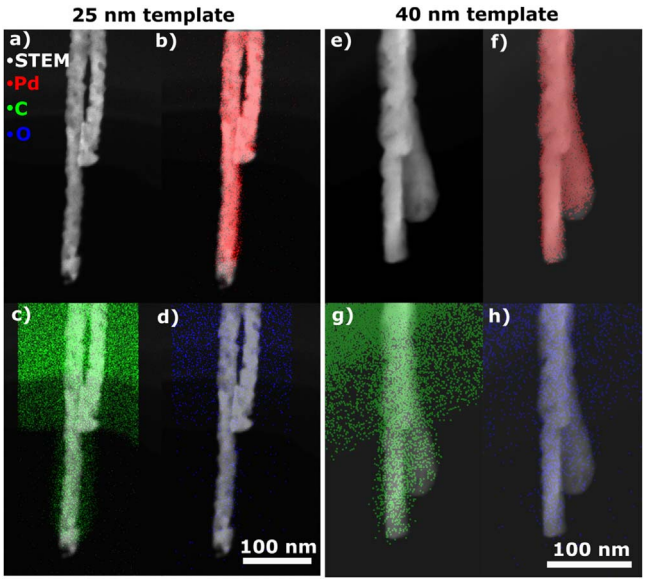

Figure 8. (a) and (e) STEM image of 25 nm and 40 nm palladium nanowire. (b) and (f) Pd Lα1 EDS maps for 25 nm and 40 nm nanowires. (c) and (g) C Kα EDS maps for 25 nm and 40 nm nanowires. (d) and (h) O Kα EDS maps for 25 nm and 40 nm nanowires.

conditions were the same for both sizes of templates, the same electrolyte was used, and the same potential pulses were applied. The only difference between the two templates is the diameter of the pores. This suggests that the observed difference in strain depends on the morphology of the template rather than the electrochemical conditions. This allows for tailoring of the strain state of the nanowires without altering the electrochemical fabrication procedure but only varying the pore diameter of the template.

High-resolution microscopy and chemical composition after removal of template.—After the growth of the palladium nanowires inside the nanoporous template the nanowires can be released by dissolving the aluminum and the alumina template in NaOH. This results in a free nanowire suspension that can be studied in the TEM by drying out a droplet of the suspension on a TEM copper grid. Figure 7 shows HR-TEM images of free nanowires with 25 nm and 40 nm diameters. The local and spatially resolved atomic structure of the nanowires is clearly made visible with TEM. The atomic structure is homogenous across the nanowires, no core–shell structure or thick amorphous layers can be seen. The Fourier transforms b) and f) of the HR-TEM images shown in Figs. 7a and 7e reveal a near-hexagonal pattern. The discrete spots in the Fourier transform indicate that the part of the nanowires within the field of view are single crystalline. This does not mean that the whole wires are single crystals, but this shows that the grains can be as large as the diameter of the nanowires. To highlight the periodic features in the HR-TEM images a Fourier filter was applied. To do this the image was transformed into reciprocal space using a fast Fourier transform (FFT) algorithm, the contrast was adjusted to highlight the frequencies of the periodic structures and then the image was transformed with an inverse FFT back to real space. Figures 7c and 7g show Fourier filtered images to highlight the periodic features in the original images. By measuring the spacing between the atomic planes visible in the image, and knowing the lattice constant of palladium, we can determine the miller index of the atomic planes. The (111) planes are clearly visible as well as the (200) planes in Fig. 7g. The difference in the measured (111) plane spacing could be due to misalignment with the zone axis. Figures 7d and 7h show TEM images of the branching end of the palladium nanowires for the 25 nm and 40 nm diameter nanowire sample, respectively. The branched pore bottoms are where crystal growth is initiated and the nanowires grow up through the branched pore bottoms. As seen, a lot of defects are present in the branches and in the region where the branches meet.

The elemental composition of the free palladium nanowires was investigated with EDS in the TEM. To gain spatial information STEM EDS mapping was used. Figure 8 shows STEM images and EDS maps of Pd Lα1, C Kα and O Kα for the 25 nm and 40 nm diameter nanowires. As seen, the palladium is evenly distributed along the wires confirming the homogeneity of the deposition. Carbon and oxygen are present on the carbon film that forms part of the TEM grid. Carbon is also found on the nanowires due to beam-induced carbon deposition from hydrocarbons in the TEM column. The copper signal that appears routinely from the TEM grid and microscope components is not shown here. Thus, the spatially resolved EDS data in Fig. 8 strengthens the argument that the wires homogeneously consist of pure palladium.

Conclusions

We have demonstrated that we can synthesise palladium nanowires of 25 nm and 40 nm in diameter through a simple templated electrochemical method. For this, electrochemical barrier layer thinning was used to make electron tunnelling through the existing oxide layer possible. When using electrochemical barrier layer thinning there is no requirement to form a delicate nanoporous membrane or evaporation of metallic contacts which simplifies the fabrication procedure. But the barrier layer thinning process results in a branched structure at the bottom of the pores which is transferred to the morphology of the palladium nanowires that adapt the shape of the pores as they grow. The branched end of the nanowires contains a large amount of structural defects revealed by TEM. Pulsed electrodeposition was used to lower the effect of mass transfer limitation which can hinder the deposition into the high aspect ratio pores. We show with the aid of simulations, the need for a short pulse duration and long off time due to mass transfer limitations caused by the low diffusion coefficient of cations in the nanoporous alumina. The synthesised nanowires are polycrystalline with a small grain size in the rage of 10–20 nm and consist of pure palladium. From XRD it was concluded that the grain size was larger along the growth direction of the nanowires and that there exists compressive strain perpendicular to the growth direction. It was also observed that the grain size and compressive strain in the nanowires depend on the size of the porous template. Smaller pores give rise to a smaller grain size and a higher compressive strain. This illustrates the effect of growing nanowires in the confined space of such nanoporous templates, which may have implications for such nanowires to be used in devices.

Acknowledgments

The diffraction experiments were performed on beamline I07 (proposal SI21922-1) at Diamond Light Source, Didcot, United Kingdom. The authors would like to thank Jonathan Rawle and Hadeel Hussein for help with the experimental setup at the I07 beamline. This work was financially supported by the Swedish Research Council through the Röntgen-Ångström Cluster "In-situ High Energy X-ray Diffraction from Electrochemical Interfaces (HEXCHEM)" (Project no. 2015-06092), and by the "Atomic Resolution Cluster"- a Research Infrastructure Fellow program of the Swedish Foundation for Strategic Research. We acknowledge financial support by NanoLund. The ex situ microscopy was performed within NanoLund at Lund University and the national centre for high-resolution electron microscopy (nCHREM) at Lund University.

ORCID

Alfred Larsson https://orcid.org/0000-0002-8932-8381

References

1. Y. Chen and A. Pepin, *Electrophoresis*, **22**, 187 (2001).
2. M. Totzeck, W. Ulrich, A. Gohnermeier, and W. Kaiser, *Nat. Photonics*, **1**, 629 (2007).
3. M. D. Austin, H. X. Ge, W. Wu, M. T. Li, Z. N. Yu, D. Wasserman, S. A. Lyon, and S. Y. Chou, *Appl. Phys. Lett.*, **84**, 5299 (2004).
4. C. T. Sousa, D. C. Leitao, M. P. Proenca, J. Ventura, A. M. Pereira, and J. P. Araujo, *Appl. Phys. Rev.*, **1** (2014).
5. W. Lee and S. J. Park, *Chem. Rev.*, **114**, 7487 (2014).
6. A. P. Li, F. Muller, A. Birner, K. Nielsch, and U. Gosele, *J. Appl. Phys.*, **84**, 6023 (1998).
7. G. Sulka, "Highly Ordered Anodic Porous Alumina Formation by Self-Organized Anodizing." *Nanostructured Materials in Electrochemistry*, ed. A. Eftekhari p. 1 (2008).
8. H. Masuda and M. Satoh, *Jpn. J. Appl. Phys.*, **2**(1b), L126 (1996).
9. K. Nielsch, F. Muller, A. P. Li, and U. Gosele, *Adv. Mater.*, **12**, 582 (2000).
10. G. Sauer, G. Brehm, S. Schneider, K. Nielsch, R. B. Wehrspohn, J. Choi, H. Hofmeister, and U. Gosele, *J. Appl. Phys.*, **91**, 3243 (2002).
11. Q. P. Wang, F. F. Min, and J. B. Zhu, *Mater. Lett.*, **91**, 9 (2013).
12. J. Zhang, G. A. Jones, T. H. Shen, S. E. Donnelly, and G. H. Li, *J. Appl. Phys.*, **101** (2007).
13. L. Zaraska, G. D. Sulka, and M. Jaskula, *Appl. Surf. Sci.*, **258**, 7781 (2012).
14. F. L. Cheng, H. Wang, Z. H. Sun, M. X. Ning, Z. Q. Cai, and M. Zhang, *Electrochem. Commun.*, **10**, 798 (2008).
15. K. T. Kim, S. J. Sim, and S. M. Cho, *IEEE Sens. J.*, **6**, 509 (2006).
16. N. Tasaltin, S. Ozturk, N. Kilinc, H. Yuzer, and Z. Z. Ozturk, *Nanoscale Res. Lett.*, **5**, 1137 (2010).
17. C. W. Xu, H. Wang, P. K. Shen, and S. P. Jiang, *Adv. Mater.*, **19**, 4256 (2007).
18. K. Nielsch, R. B. Wehrspohn, J. Barthel, J. Kirschner, U. Gosele, S. F. Fischer, and H. Kronmuller, *Appl. Phys. Lett.*, **79**, 1360 (2001).
19. G. Slaughter and T. Kulkarni, *Microelectron. Eng.*, **149**, 92 (2016).
20. G. D. Sulka, A. Brzozka, L. Zaraska, and M. Jaskula, *Electrochim. Acta*, **55**, 4368 (2010).
21. G. Sharma, M. V. Pishko, and C. A. Grimes, *J. Mater. Sci.*, **42**, 4738 (2007).
22. L. Zaraska, G. D. Sulka, and M. Jaskula, *J Solid State Electr*, **15**, 2427 (2011).
23. W. J. Stepniowski, W. Florkiewicz, M. Michalska-Domanska, M. Norek, and T. Czujko, *J. Electroanal. Chem.*, **741**, 80 (2015).
24. D. A. Bograchev, V. M. Volgin, and A. D. Davydov, *Electrochim. Acta*, **96**, 1 (2013).
25. E. A. Bluhm, E. Bauer, R. M. Chamberlin, K. D. Abney, J. S. Young, and G. D. Jarvinen, *Langmuir*, **15**, 8668 (1999).
26. K. S. Napolskii, I. V. Roslyakov, A. A. Eliseev, D. I. Petukhov, A. V. Lukashin, S. F. Chen, C. P. Liu, and G. A. Tsirlina, *Electrochim. Acta*, **56**, 2378 (2011).
27. J. Azevedo, C. T. Sousa, A. Mendes, and J. P. Araujo, *J Nanosci Nanotechno*, **12**, 9112 (2012).
28. N. A. Vinogradov, G. S. Harlow, F. Carla, J. Evertsson, L. Rullik, W. Linpe, R. Felici, and E. Lundgren, *ACS Appl. Nano Mater.*, **1**, 1265 (2018).
29. J. Evertsson, N. A. Vinogradov, G. S. Harlow, F. Carla, S. R. McKibbin, L. Rullik, W. Linpe, R. Felici, and E. Lundgren, *RSC Adv.*, **8**, 18980 (2018).
30. W. Linpe, G. S. Harlow, J. Evertsson, U. Hejral, G. Abbondanza, F. Lenrick, S. Seifert, R. Felici, N. A. Vinogradov, and E. Lundgren, *ACS Appl. Nano Mater.*, **2**, 3031 (2019).
31. G. S. Harlow, J. Drnec, T. Wiegmann, W. Lipe, J. Evertsson, A. R. Persson, R. Wallenberg, E. Lundgren, and N. A. Vinogradov, *Nanoscale Adv*, **1**, 4764 (2019).
32. P. P. Mardilovich, A. N. Govyadinoy, N. I. Mazurenko, and R. Paterson, *J. Membr. Sci.*, **98**, 143 (1995).
33. J. Abys, "Palladium Electroplating." *Modern Electroplating*, ed. M. Schlesinger and M. Paunovic p. 327 (2011).
34. M. S. Chandrasekar and M. Pushpavanam, *Electrochim. Acta*, **53**, 3313 (2008).
35. C. A. Schneider, W. S. Rasband, and K. W. Eliceiri, *Nat. Methods*, **9**, 671 (2012).
36. E. Vlieg, *J. Appl. Crystallogr.*, **31**, 198 (1998).
37. U. Welzel, J. Ligot, P. Lamparter, A. C. Vermeulen, and E. J. Mittemeijer, *J. Appl. Crystallogr.*, **38**, 1 (2005).
38. K. Nielsch, J. Choi, K. Schwirn, R. B. Wehrspohn, and U. Gosele, *Nano Lett.*, **2**, 677 (2002).
39. C. M. Schleputz, S. O. Mariager, S. A. Pauli, R. Feidenhans'l, and P. R. Willmott, *J. Appl. Crystallogr.*, **44**, 73 (2011).
40. B. Benfedda, L. Hamadou, N. Benbrahim, A. Kadri, E. Chainet, and F. Charlot, *J. Electrochem. Soc.*, **159**, C372 (2012).
41. M. Nehra, A. N. Dilbaghi, V. Singh, N. K. Singhal, and S. Kumar, *Physica Status Solidi (a)*, **217**, 1900842 (2020).
42. C. Frantz, C. Vichery, J. Zechner, D. Frey, G. Burki, H. Cebeci, J. Michler, and L. Philippe, *Appl. Surf. Sci.*, **330**, 39 (2015).
43. A. W. Hassel and M. M. Lohrengel, *Electrochim. Acta*, **40**, 433 (1995).
44. J. K. Novev and R. G. Compton, *Curr Opin Electroche*, **7**, 118 (2018).
45. D. M. Smilgies, *J. Appl. Crystallogr.*, **42**, 1030 (2009).